

## **Robust Magnetoelectric Effect in Decorated Graphene/In<sub>2</sub>Se<sub>3</sub> Heterostructure**

Shang, J.; Tang, X.; Gu, Y.; Krasheninnikov, A.; Picozzi, S.; Chen, C.; Kou, L.;

Originally published:

January 2021

**ACS Applied Materials and Interfaces 13(2021), 3033-3039**

DOI: <https://doi.org/10.1021/acsami.0c19768>

Perma-Link to Publication Repository of HZDR:

<https://www.hzdr.de/publications/Publ-32421>

Release of the secondary publication  
on the basis of the German Copyright Law § 38 Section 4.

# Robust Magnetoelectric Effect in Decorated Graphene/In<sub>2</sub>Se<sub>3</sub> Heterostructure

Jing Shang<sup>1</sup>, Xiao Tang<sup>1</sup>, Yuantong Gu<sup>1</sup>, Arkady V. Krasheninnikov<sup>2,3</sup>, Silvia Picozzi<sup>4\*</sup>, Changfeng Chen<sup>5\*</sup>, Liangzhi Kou<sup>1\*</sup>.

<sup>1</sup> School of Mechanical, Medical and Process Engineering, Queensland University of Technology, Brisbane, QLD 4001, Australia

<sup>2</sup> Institute of Ion Beam Physics and Materials Research, Helmholtz-Zentrum Dresden-Rossendorf, 01328 Dresden, Germany

<sup>3</sup> Department of Applied Physics, Aalto University School of Science, Aalto FI-00076, Finland

<sup>4</sup> Consiglio Nazionale Delle Ricerche, Istituto SPIN, UOS l'Aquila, Sede di Lavoro CNR-SPIN C/o Università G. d'Annunzio, Chieti, 66100, Italy

<sup>5</sup> Department of Physics and Astronomy, University of Nevada, Las Vegas, Nevada 89154, United States

## Corresponding Author

\*E-mail: [silvia.Picozzi@spin.cnr.it](mailto:silvia.Picozzi@spin.cnr.it)

\*E-mail: [chen@physics.unlv.edu](mailto:chen@physics.unlv.edu)

\*E-mail: [liangzhi.kou@qut.edu.au](mailto:liangzhi.kou@qut.edu.au)

**ABSTRACT.** Magnetoelectric effect is a fundamental physical phenomenon that synergizes electric and magnetic degrees of freedom to generate distinct material responses like electrically tuned magnetism, which serves as a key foundation of the emerging field of spintronics. Here, we show by first-principles studies that ferroelectric (FE) polarization of an  $\text{In}_2\text{Se}_3$  monolayer can modulate the magnetism of an adjacent transition-metal (TM) decorated graphene layer via a ferroelectrically induced electronic transition. The TM nonbonding  $d$ -orbital shifts downward and hybridizes with carbon- $p$  states near the Fermi level, suppressing the magnetic moment, under one FE polarization, but on reversed FE polarization this TM  $d$ -orbital moves upward, restoring the original magnetic moment. This finding of robust magnetoelectric effect in TM decorated graphene/ $\text{In}_2\text{Se}_3$  heterostructure offers powerful insights and a promising avenue for experimental exploration of ferroelectrically controlled magnetism in 2D materials.

**KEYWORDS:** TM decorated graphene/ $\text{In}_2\text{Se}_3$  heterostructure; Magnetoelectric effect;  $d$ -orbital shifts; First-principles calculations.

Low-dimensional magnetic materials provide excellent platforms for spintronics that use electron spin rather than charge as the information carrier, and recent years have seen tremendous developments in this emerging field that promises equipment with higher storage density and lower energy consumption<sup>1-3</sup>. Prototypical spintronic devices have been proposed and demonstrated<sup>4-6</sup>, but further advances in the field have been hindered by a lack of suitable low-dimensional magnetic materials and adequate means for effective tuning of their magnetic behaviour. Recent studies have reported synthesis of atomically thin 2D magnets, such as CrI<sub>3</sub><sup>7</sup>, CrGeTe<sub>3</sub><sup>8</sup>, Fe<sub>3</sub>GeTe<sub>2</sub><sup>9</sup> and Fe<sub>2</sub>O<sub>3</sub><sup>10</sup>; but these materials have low Curie temperatures (~ 45 K) that limit the scope of their viability. Meanwhile, graphene as the first discovered truly 2D material<sup>11</sup> has been explored for its magnetic properties<sup>12</sup>, and magnetism was observed in transition-metal (TM) decorated graphene<sup>13-19</sup> induced by the hybridization of carbon *p* and TM-*d* orbitals<sup>20,21</sup>. Especially notable is the synthesis of suspended TM decorated single vacancy graphene (TM@SVG) monolayer<sup>22,23</sup> with considerably improved stability of well dispersed TM atoms.

Effective control of magnetism in low-dimensional materials by reliable and convenient means is an essential requirement in spintronics. Among various strategies, electric-field controlled magnetism is regarded as the most promising<sup>24-28</sup>. There are three main material-class specific working mechanisms<sup>28</sup>: (i) magnetic exchange modulation by electrically tuneable carrier concentration in magnetic semiconductors, (ii) changing coercivity or magnetic anisotropy by shifting the Fermi level in magnetic metals, and (iii) magnetic response to electric tuning via magnetoelectric coupling in multiferroics. Major challenges remain, however, in identifying suitable low-dimensional, mainly 2D, materials with robust magnetism that is responsive to electric-field tuning. An important development on this front is the recently reported synthesis of In<sub>2</sub>Se<sub>3</sub> monolayer that has proven to be a versatile platform for designing and implementing 2D ferroelectric (FE) based non-volatile memory devices<sup>29,30</sup> and also for facilitating diverse chemical and physical processes, such as photocatalytic water splitting<sup>31</sup> and magnetic anisotropy modulations<sup>32</sup>.

In this letter, we present computational evidence for robust magnetoelectric effect in viable TM@SVG/In<sub>2</sub>Se<sub>3</sub> heterostructures, allowing for effective electric tuning of magnetism. First-principles calculations show that magnetic moments derived from TM atoms adsorbed on SVG (V, Cr, Mn@SVG) are highly sensitive to, and therefore effectively controllable by, the switch of FE polarization of the In<sub>2</sub>Se<sub>3</sub> monolayer. This intriguing phenomenon stems from an FE-induced electronic transition that shifts the originally unoccupied nonbonding TM-*d* states toward the Fermi level to hybridize with the carbon-derived states, thereby largely suppressing the magnetic moment, while a reversal of FE polarization restores the original magnetic state. This electric modulation of magnetism relies on the strong characters of FE polarization of In<sub>2</sub>Se<sub>3</sub> monolayer, which exerts FE-

sensitive electrostatic potentials and associated electron transfers across the interface in the heterostructure. These findings unveil a distinct mechanism for compelling FE controlled magnetism, making TM@SVG/In<sub>2</sub>Se<sub>3</sub> a promising platform for exploring new magnetoelectric effects in advanced spintronics materials research.

Spin-polarized electronic structures and total energy calculations have been performed using the Vienna Ab-initio Simulation Package (VASP)<sup>33, 34</sup>. Computational details are provided in the Supplemental Material. The TM@SVG/In<sub>2</sub>Se<sub>3</sub> heterostructure is constructed by matching a 5×5×1 supercell of SVG with a 3×3×1 supercell of In<sub>2</sub>Se<sub>3</sub> monolayer, as shown in Fig. 1 (a-b). The lattice mismatch in this structural model is 0.14%, which has only minimal effects on the computed total energies, structural and electronic properties; this result is also demonstrated by applying the lattice mismatch strain on In<sub>2</sub>Se<sub>3</sub> but keeping graphene strain free, see Fig. S1. To describe the on-site Coulomb interaction, the Hubbard parameter  $U_{\text{eff}}$  is taken as 4 eV for all the transition metals based on previously reported results<sup>35-37</sup> and our tests shown in Fig. S2. The In<sub>2</sub>Se<sub>3</sub> monolayer has two distinct faces in contact with graphene, with the FE polarization either pointing upward (P $\uparrow$ ) or downward (P $\downarrow$ ), as defined in Fig. 1(b).

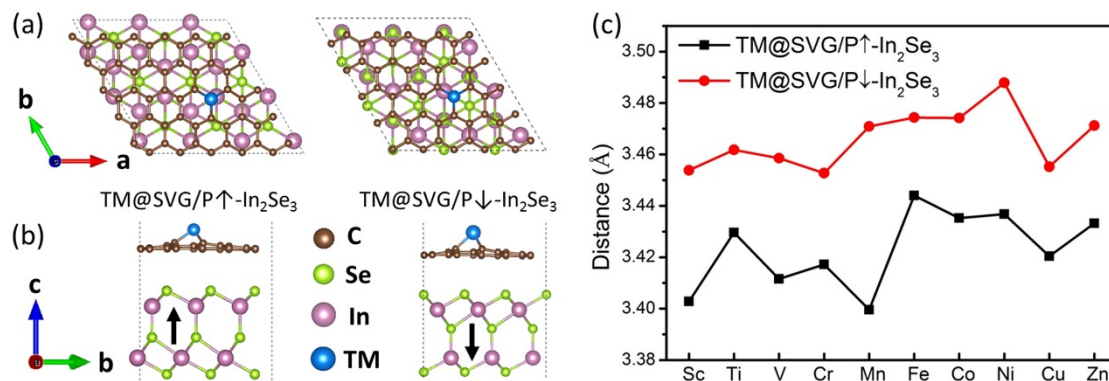


Fig. 1 Atomic configurations in (a) top and (b) side view of TM@SVG/In<sub>2</sub>Se<sub>3</sub> heterostructure with the ferroelectric polarizations in two characteristic directions, defined as up and down, indicated by the black arrows in (b). Results in (c) show the distances between the TM@SVG with various TM atoms and In<sub>2</sub>Se<sub>3</sub> monolayer in two distinct polarizations.

We first examined TM decorated graphene on In<sub>2</sub>Se<sub>3</sub> (TM@graphene/In<sub>2</sub>Se<sub>3</sub>), where the TM atom is adsorbed at the energetically most preferred hexagonal hollow site [see Fig. S2 (a-b)], and the FE polarization switch of In<sub>2</sub>Se<sub>3</sub> monolayer produces obvious effects on the total magnetic moments of the system [Fig. S2 (d)]. For Cr or Mn, the magnetic moments are 0  $\mu$ B at TM@graphene/P $\uparrow$ -In<sub>2</sub>Se<sub>3</sub> but become  $\sim$  4.5  $\mu$ B at TM@graphene/P $\downarrow$ -In<sub>2</sub>Se<sub>3</sub> (these magnetic moments are reduced slightly by

on-site Coulomb interaction, see Fig. S2 (c). These results demonstrate significant tunability of FE controlled magnetism. However, TM atoms adsorbed on graphene have low migration energy barriers ( $0.2\sim 0.8$  eV<sup>21</sup>) that creates a strong tendency for TM atoms to migrate and form metal clusters, which is detrimental to the stability and functionality of TM@graphene/In<sub>2</sub>Se<sub>3</sub>. A promising resolution to this issue is offered by the recently synthesized suspended TM@SVG layered structure where the TM atom bonds strongly to the otherwise under-coordinated carbon atoms near the vacancy site in the graphene layer, thus greatly enhancing the stability of the dispersed TM atom configuration and making TM@SVG a viable layered magnetic structure, which can be used to form functional heterostructures with In<sub>2</sub>Se<sub>3</sub> monolayer. The large diffusion barrier up to 6.8 and 4.5eV for P $\uparrow$  and P $\downarrow$  configurations respectively (taking Mn@SVG/In<sub>2</sub>Se<sub>3</sub> as an example, see Fig. S3) can effectively prevent the formation of TM clusters on the surface. Our calculations show that TM atoms in TM@SVG take out-of-layer equilibrium positions due to its larger radius compared to carbon, which is consistent with previous reports<sup>20, 21</sup>. Meanwhile, the interlayer distance between graphene and In<sub>2</sub>Se<sub>3</sub> is sensitive to the FE polarization of the latter [Fig. 1 (c)], which reflects the distinct nature of the FE-dependent interlayer interaction and has profound effects on key properties of the heterostructure as will be discussed below. TM atoms can locate either on top of graphene [Fig. 1(a-b)] or between the graphene and In<sub>2</sub>Se<sub>3</sub> layers [Mn@SVG/In<sub>2</sub>Se<sub>3</sub> is shown as an example in Fig. S4 (a-b)] since both configurations are stable based on calculated formation energies. However, a TM atom is hard to diffuse from top to interlayer positions or vice vice due to the very large diffusion barrier (2.68 eV or 3.88 eV) for the crossing of TM atoms (from Mn1 to Mn10) as shown in Fig. S5. Meanwhile the small diffusion coefficient for the TM atom migration on defective graphene<sup>21, 38</sup> as measured by experiments prevents TM atoms moving from top to interlayer positions. Since the electronic and magnetic properties of both configurations are the same (see Fig. S4), in the following discussion, we mainly focus on the configurations with TM atoms on top of graphene.

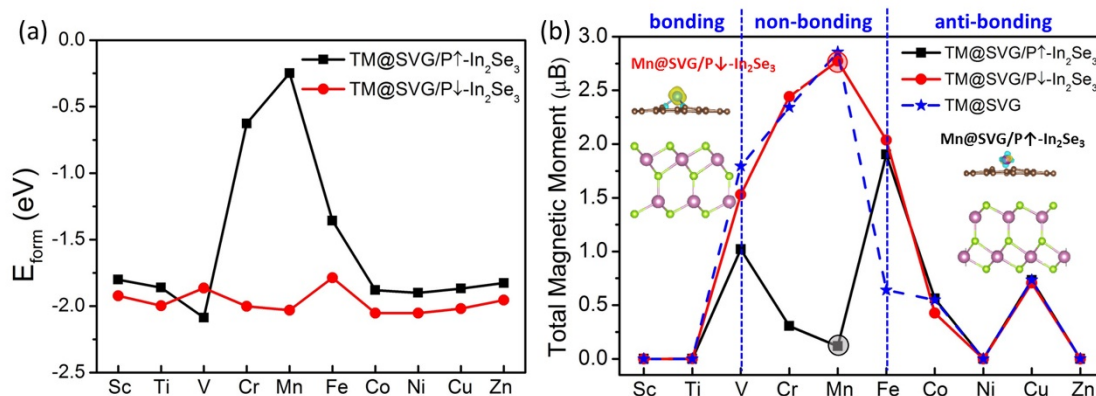


Fig. 2 (a) Formation energy of TM@SVG for various TM atoms and In<sub>2</sub>Se<sub>3</sub> monolayer in up (P $\uparrow$ ) or down (P $\downarrow$ ) FE polarization. (b) Total magnetic moment  $M$  ( $\mu\text{B}$ ) of TM@SVG/In<sub>2</sub>Se<sub>3</sub> heterostructures. Insets show the spin density of Mn@SVG/In<sub>2</sub>Se<sub>3</sub> with both FE polarizations in In<sub>2</sub>Se<sub>3</sub>, where the isosurface is set to  $0.03$  eV/ $\text{\AA}^3$ .

To assess the stability of TM@SVG/In<sub>2</sub>Se<sub>3</sub> heterostructures and the influence of the FE polarization in the In<sub>2</sub>Se<sub>3</sub> monolayer, we have calculated formation energy  $E_{\text{form}} = E_{\text{total}} - E_{\text{TM@SVG}} - E_{\text{In}_2\text{Se}_3}$ , where  $E_{\text{total}}$ ,  $E_{\text{TM@SVG}}$ , and  $E_{\text{In}_2\text{Se}_3}$  are, respectively, the energy of the heterostructure, freestanding TM@SVG, and In<sub>2</sub>Se<sub>3</sub> monolayer. This quantity measures the interaction between the TM@SVG and In<sub>2</sub>Se<sub>3</sub> layers, and the calculated results for all the studied TM cases are negative as shown in Fig. 2(a), indicating that these heterostructures are viable. It is noted that formation energies of TM@SVG/P↓-In<sub>2</sub>Se<sub>3</sub> are generally larger than those with P↑ FE polarization, except for V@SVG/In<sub>2</sub>Se<sub>3</sub>. For most TM@SVG cases, differences in formation energy with P↓ and P↑ polarizations are small, around 0.1 eV, but two outstanding cases, (Cr, Mn)@SVG/In<sub>2</sub>Se<sub>3</sub>, exhibit considerably larger differences in polarization dependent formation energy, up to 1.5 ~ 2 eV, indicating strong contrasting effects by the opposite FE states in the In<sub>2</sub>Se<sub>3</sub> monolayer. It should be noted that, although some of the formation energies are small, they indicate the relative weak interlayer interaction, the transition atoms are strongly connected with surrounding C atoms as shown by the large the TM-C interaction, short bond lengths and strong ionic bonding (Fig. S6) regardless of the polarization direction.

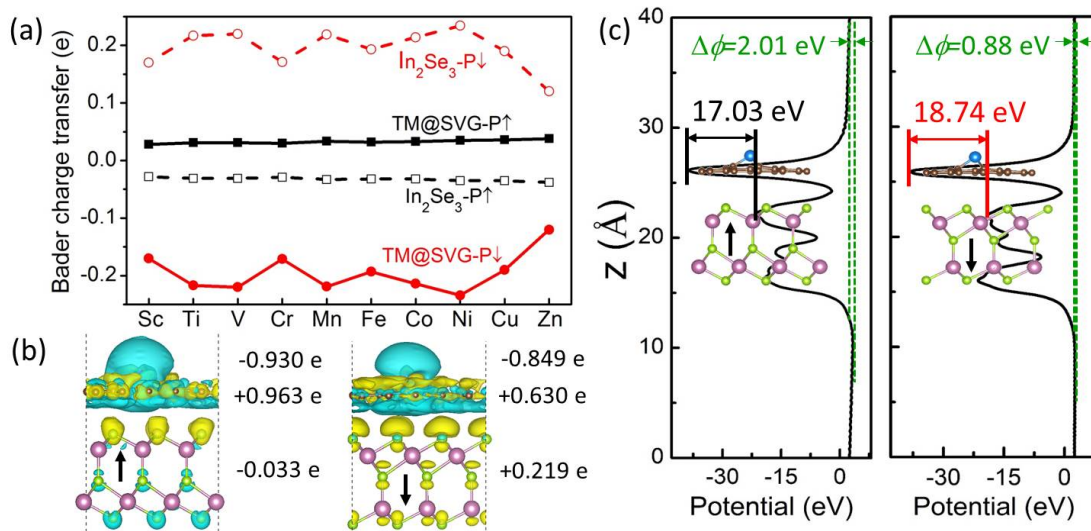


Fig. 3 (a) Electron transfer based on a Bader charge analysis between TM@SVG and In<sub>2</sub>Se<sub>3</sub> layers in TM@SVG/In<sub>2</sub>Se<sub>3</sub> heterostructures. (b) The differential charge density of Mn@SVG/In<sub>2</sub>Se<sub>3</sub> heterostructures with P↑ and P↓ FE polarization in the In<sub>2</sub>Se<sub>3</sub> layer. The isosurface value is set to 0.0002 eV/Å<sup>3</sup>. (c) The electrostatic potential profile for Mn@SVG/In<sub>2</sub>Se<sub>3</sub> and the potential differences between graphene and contacting In atoms for the two polarizations. Vertical green lines are plotted to indicate the electrostatic potential difference for opposite sides of the heterostructure.

We now evaluate the FE polarization dependence of magnetic properties of TM@SVG/In<sub>2</sub>Se<sub>3</sub>. The total magnetic moments with the In<sub>2</sub>Se<sub>3</sub> layer in P↑ or P↓ FE polarizations are displayed in Fig. 2(b),

compared with the results for freestanding TM@SVG. It has been proposed<sup>20</sup> that these TM@SVG systems mainly fall into three categories: bonding (Sc, Ti), nonbonding (V, Cr, Mn) and antibonding (Co, Ni, Cu, Zn), while Fe represents a special case, sitting between nonbonding and antibonding regimes and exhibiting complex magnetic behaviours. Our calculated results shown in Fig. 2 (b) indicate that (i) In<sub>2</sub>Se<sub>3</sub> in P<sub>↓</sub> polarization has little influence on the magnetic moments of the TM@SVG studied here, with the only exception for Fe@SVG, all of which nearly coincide with result of the freestanding TM@SVG layer; (ii) for the bonding cases, the TM-*d* orbitals are fully occupied, rendering zero magnetic moment, independent of the FE polarization of In<sub>2</sub>Se<sub>3</sub>, and for the antibonding cases, the results for TM@SVG/P<sub>↓</sub>-In<sub>2</sub>Se<sub>3</sub>, TM@SVG/P<sub>↑</sub>-In<sub>2</sub>Se<sub>3</sub> and freestanding TM@SVG all stay very close; (iii) the nonbonding cases of V, Cr and Mn@SVG/In<sub>2</sub>Se<sub>3</sub> possess magnetic moments that are sensitively dependent on the FE polarization of In<sub>2</sub>Se<sub>3</sub>. For example, the magnetic moment is 2.9 μB at Mn@SVG/P<sub>↓</sub>-In<sub>2</sub>Se<sub>3</sub>, but only 0.12 μB at Mn@SVG/P<sub>↑</sub>-In<sub>2</sub>Se<sub>3</sub>. It is worth noting that the total magnetic moments in TM@SVG/In<sub>2</sub>Se<sub>3</sub> systems are mainly contributed by TM atoms while a small portion of magnetic moments comes from the three nearest carbon atoms with opposite spin polarization (the values on TM and carbon atoms are shown in Fig. S7). To probe the origin of these sharply contrasting behaviours, we have artificially tuned the distance between Mn@SVG and In<sub>2</sub>Se<sub>3</sub> layers to test the influence of the interlayer interaction, and the results [see Fig. S8] show that the magnetic moment of Mn@SVG/P<sub>↑</sub>-In<sub>2</sub>Se<sub>3</sub> increases with the rising interlayer distance, suggesting strong interlayer effect on the magnetism on Mn@SVG layer, and the value approaches that of the freestanding TM@SVG at large interlayer distances when the effect of the In<sub>2</sub>Se<sub>3</sub> layer on the TM@SVG diminishes. Meanwhile, the magnetic moment of Mn@SVG/P<sub>↓</sub>-In<sub>2</sub>Se<sub>3</sub> remains largely unchanged throughout this process, indicating little influence by the interlayer interaction. The FE polarization dependent magnetism is also seen in spatial spin distributions, where a larger amount of unpaired electrons gather around the Mn site in the case of Mn@SVG/P<sub>↓</sub>-In<sub>2</sub>Se<sub>3</sub>, while a much smaller spin density appears in the case of Mn@SVG/P<sub>↑</sub>-In<sub>2</sub>Se<sub>3</sub> [see insets of Fig. 2(b)].

To check the dependence of the calculated interlayer interaction and associated magnetic behaviours on the choice of the vdW potential, we have performed additional calculations using the Tkatchenko-Scheffler (TS) and DFT-D3 method with Becke-Jonson damping methods. For the exemplary case of Mn@SVG/In<sub>2</sub>Se<sub>3</sub>, we find that although the magnitude of magnetic moments does vary quantitatively with the choice of potentials, the overall behaviours remain unchanged (for details see the results presented in Table S1).

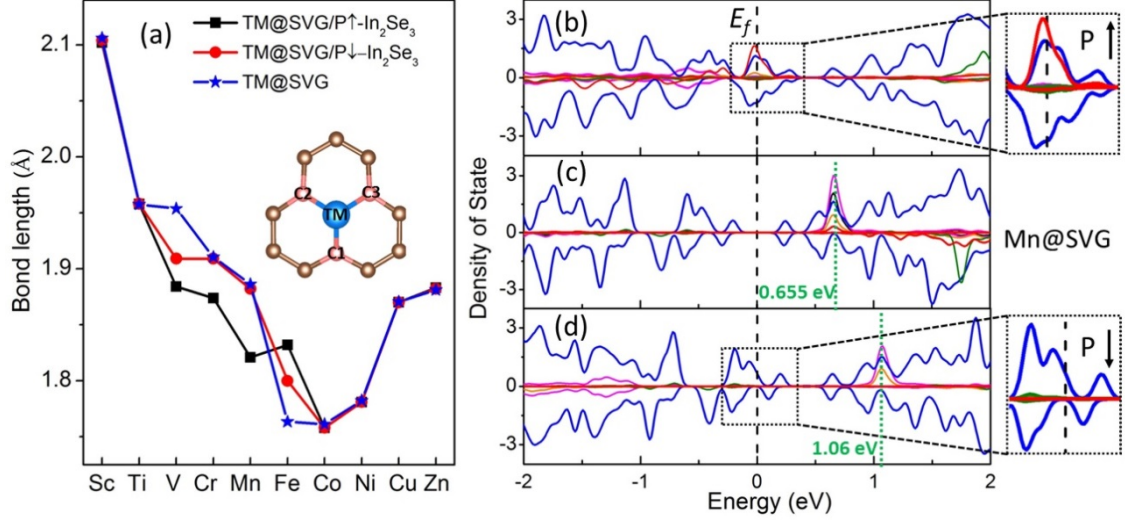


Fig. 4 (a) The bond length between the TM atom and the nearest-neighbour carbon atoms (inset shows the structural configuration) in the TM@SVG/In<sub>2</sub>Se<sub>3</sub> heterostructure with distinct FE polarizations and in the freestanding TM@SVG. (b-d) Spin polarized (positive/negative values for up/down spin) electronic density of states; blue and red lines represent contributions from the carbon-*p<sub>z</sub>* and Mn-*d<sub>x<sup>2</sup>-y<sup>2</sup></sub>* orbitals.

The sharply contrasting behaviours of the formation energy and magnetic responses of the TM@SVG/In<sub>2</sub>Se<sub>3</sub> heterostructures presented above can be understood in terms of the interfacial charge transfer and the resulting shift of the TM *d* orbital under distinct FE polarizations of the In<sub>2</sub>Se<sub>3</sub> monolayer. The results of a Bader charge analysis [Fig. 3(a)] indicate that opposite FE polarizations have significantly distinct influence on the electron transfer between the TM@SVG and In<sub>2</sub>Se<sub>3</sub> layers. When In<sub>2</sub>Se<sub>3</sub> is in the P↑ polarization, only 0.03 *e* is transferred to TM@SVG from In<sub>2</sub>Se<sub>3</sub>, which acts as an electron donor. In sharp contrast, In<sub>2</sub>Se<sub>3</sub> becomes an electron acceptor to receive a much larger amount (~ 0.2 *e*) of charge transfer from the TM@SVG layer when the polarization is reversed to P↓. This drastically increased electron transfer leads to much stronger interfacial interaction, as reflected in the greatly enhanced formation energy [Fig. 2(a)]. For an intuitive understanding, we take Mn@SVG/In<sub>2</sub>Se<sub>3</sub> as an example to analyse the spatial charge density difference  $\Delta\rho = \rho_{\text{total}} - \rho_{\text{In}_2\text{Se}_3} - \rho_{\text{SVG}} - \rho_{\text{Mn}}$ . The results [Fig. 3(b)] show that in P↑-In<sub>2</sub>Se<sub>3</sub> electron transfer occurs mostly from the Mn atom to SVG with only a minimal amount from the In<sub>2</sub>Se<sub>3</sub> monolayer, whereas in P↓-In<sub>2</sub>Se<sub>3</sub> there is a considerable amount of electron transfer from the Mn atom to the In<sub>2</sub>Se<sub>3</sub> monolayer through the contacting SVG layer. This result can be ascribed to the larger electrostatic potential difference (18.74 eV versus 17.03 eV) at the interfaces of the heterostructure as shown in Fig. 3(c), and also electrostatic potential differences on the opposite sides of the heterostructures (2.01 eV vs 0.88 eV) due to the FE polarizations in In<sub>2</sub>Se<sub>3</sub> layers, where the surface of the In<sub>2</sub>Se<sub>3</sub> monolayer with lower electrostatic potential is in close contact with the Mn@SVG layer.

The FE controlled magnetic behaviours [Fig. 2(b)] can be further elucidated by examining pertinent chemical bonding changes and the spin polarized density of states of the adsorbed TM atom under

different polarizations of the  $\text{In}_2\text{Se}_3$  monolayer. Since most of the magnetic moment is contributed by the TM and surrounding carbon atoms, it is instructive to analyse the TM-C bond length and the associated band shifts. We show in Fig. 4(a) the calculated TM-C bond length, and the results indicate that the TM-C bond length first follows a descending trend in going from 2.10 Å (Sc) to 1.75 Å (Co), and then moves upward and increases to 1.90 Å (Zn); the same trend is seen in freestanding TM@SVG. For most cases, the bond lengths between the adsorbed TM atom and the three nearest-neighbour carbon atoms remain nearly unchanged under the switch of FE polarization, so the  $C_{3v}$  symmetry at the TM-adsorbed carbon vacancy site in SVG is preserved during the FE switch. Notable differences, however, exist in the TM-C bond length for the cases involving the nonbonding states (V, Cr, Mn). This pattern in bond-length variations corroborates with the behaviours of the magnetic modulation by FE polarization [Fig. 2(b)]. These shorter TM-C bonds enhance the hybridization between the TM- $d$  and carbon- $p$  states, thereby asserting stronger influence on the magnetic moment of the TM@SVG- $\text{In}_2\text{Se}_3$  heterostructure.

For a more in-depth assessment of the driving mechanism for the magnetic responses, we have examined the partial density of state (PDOS) of the Mn- $d$  orbital and its hybridization with the  $p$  orbitals of the surrounding nearest-neighbour carbon atoms. Calculated spin-polarized PDOS for Mn@SVG/ $\text{In}_2\text{Se}_3$  in both polarizations are shown in Fig. 4 (c), together with the results for freestanding Mn@SVG for comparison. It is seen that in Mn@SVG/ $P\uparrow$ - $\text{In}_2\text{Se}_3$ , the shortening of the Mn-C bonds leads to a large downward shift of the Mn- $d$  orbital, which is located 0.655 eV above the Fermi level in freestanding Mn@SVG, to the vicinity of the Fermi level. As a result, the originally unoccupied nonbonding Mn- $d$  state is now partially occupied and hybridizes with the nearest C- $p$  states near the Fermi level. This large shifting of the Mn- $d$  state considerably reduces the spin spitting and, therefore the associated magnetic moment. Similar mechanisms have been invoked in previous studies<sup>39, 40</sup> to explain the relationship between carbon vacancies and the induced magnetism. In sharp contrast, after the FE polarization of the heterostructure is switched to the reversed direction, the Mn- $d$  state in Mn@SVG/ $P\downarrow$ - $\text{In}_2\text{Se}_3$ ) moves upward in energy from its original position to be further away, located at 1.06 eV above the Fermi level, accompanied by a slight shift of the C- $p$  states toward the Fermi level. Under this circumstance, there is no hybridization between the Mn- $d$  and C- $p$  orbitals, and the pertinent nonbonding Mn- $d$  state remains unoccupied, thus leaving the magnetic moment of the heterostructure unaffected in  $P\downarrow$ - $\text{In}_2\text{Se}_3$ , despite the resulted increase in the spin splitting of the Mn- $d$  states. To confirm the reliability of the analysis about orbital hybridization, we calculated the DOS and magnetic properties of freestanding  $3\times 3\times 1$  Mn@SVG [shown in Fig. S9 (a)] using the HSE<sup>41</sup> functional to verify if the standard PBE results can capture the main underlying physics. The total spin moment of freestanding Mn@SVG is 2.679  $\mu_B$  calculated using the HSE functional, which is the same as the PBE result. Besides, the spin polarized partial DOS plotted in Fig. S9 (b) shows no hybridization between the Mn- $d$  and C- $p$  orbitals near the Fermi level, therefore the pertinent

nonbonding Mn-*d* state remains unoccupied and results in the magnetic moment for Mn@SVG. These results indicate that PBE simulations can well capture the main physics, and the findings reported here are reliable. This mechanism also renders similar phenomena of FE polarization modulation in Cr@SVG/In<sub>2</sub>Se<sub>3</sub> (see Fig. S10). In the P↑ FE polarization of the In<sub>2</sub>Se<sub>3</sub> monolayer, the Cr-*d* state shifts downward toward the Fermi level and hybridizes with the C-*p* states, resulting in the diminished total magnetic moment in the heterostructure. In contrast, when the FE polarization is reserved to P↓, the nonbonding Cr-*d* state moves upward and remains unoccupied, thus not affecting the magnetism. These results suggest that the reversible FE polarization of In<sub>2</sub>Se<sub>3</sub> monolayer can act as an effective control for magnetism of TM@SVG in a heterostructure configuration, which is highly promising for feasible and convenient modulation of 2D magnetism that may facilitate innovative design and implementation in novel spintronic operations.

The phenomena revealed here, namely the ferroelectric controlled magnetism and magnetoelectronic coupling in the 2D heterostructures are interesting and promising for the next generation spintronic devices. However, for practical applications, several issues still need to be discussed and solved, such as the detection of magnetic orders in low-dimensional materials and the polarization reversal in ferroelectrics. Recent experimental developments have laid solid foundations for the magnetic detection and ferroelectric control. For example, effective probing strategies have been developed to characterize and detect the magnetization in 2D magnets<sup>7, 8</sup> such as Magneto-Optical Kerr effect (MOKE)<sup>42</sup>, Raman, second harmonic generation, reflection magnetic circular dichroism, polarization-resolved photoluminescence from a proximity layer and scanning single-spin magnetometry based on nitrogen-vacancy (NV) centre<sup>43</sup>. These technological achievements render magnetic detection and manipulation of TM doped graphene feasible.

Magnetic control in the heterostructure depends on the polarization reversal of ferroelectrics. The recent experimental synthesis of In<sub>2</sub>Se<sub>3</sub> nanoflake on the substrate and polarization manipulations provided feasibility of ferroelectric switch by an external electric field<sup>30</sup>. The charge transfers between In<sub>2</sub>Se<sub>3</sub> and substrates, and expected energy differences between two polarization states share very similar reversal mechanism with the TM@SVG/In<sub>2</sub>Se<sub>3</sub> heterostructure in the present work. The critical electric field for switched polarizations of ~1.5 V<sup>30</sup> renders the polarization switch highly possible.

For practical applications, the effects of environments on the magnetic behaviours and associated tunability need to be evaluated. We checked the influence of O<sub>2</sub> and H<sub>2</sub>O molecule adsorptions on the magnetic states of Mn@SVG/In<sub>2</sub>Se<sub>3</sub> as typical examples and found that the adsorption of O<sub>2</sub> molecules would change the magnetic behaviours in Mn@SVG-P↑-In<sub>2</sub>Se<sub>3</sub>, but the Mn@SVG-P↓-In<sub>2</sub>Se<sub>3</sub> stays unchanged, as shown in Fig. S11 (a-b). Meanwhile, H<sub>2</sub>O molecules have no obvious effect on the magnetism of Mn@SVG-In<sub>2</sub>Se<sub>3</sub> systems, see Fig. S11 (c-d). Therefore, the magnetic

manipulation of these heterostructures would be most robust in a vacuum without any oxygen environment, but the tuneable magnetism can survive when water molecules are present.

In summary, we find robust magnetoelectric effect in TM@SVG/In<sub>2</sub>Se<sub>3</sub> heterostructures based on the results of systematic first-principles calculations. Our extensive computational studies show that switching the FE polarization in In<sub>2</sub>Se<sub>3</sub> monolayer can effectively modulate the magnetic moment in the adjacent TM@SVG layer, thereby realizing a long-sought platform for feasible experimental exploration of effective electric control of magnetism. An analysis of the interfacial bonding and charge transfer in the heterostructure reveals sensitive dependence of the charge and spin polarizations that concurrently impact the FE and magnetic order in the system. In particular, the nonbonding TM-*d* state originally located above the Fermi level in freestanding TM@SVG shifts in opposite directions under the influence of different FE polarizations. In response to P↓-In<sub>2</sub>Se<sub>3</sub>, the TM-*d* state moves further away from the Fermi level, enhancing the spin splitting but not altering the magnetic moment, while under P↑-In<sub>2</sub>Se<sub>3</sub>, the TM-*d* state drops below the Fermi level, becoming partially occupied and hybridizing with carbon-*p* states, which considerably reduces the spin splitting of the TM-*d* states and the associate dominant contributions to the magnetic moment. Since freestanding magnetic TM@SVG and ferroelectric In<sub>2</sub>Se<sub>3</sub> monolayer structures both have been experimentally synthesized and characterized, it is reasonable to expect that the construction of the heterostructure based on these 2D materials is practically feasible. The intricate working mechanisms unveiled in the present work may help develop other layered material structures in the fast growing family of 2D materials possessing diverse electric and magnetic behaviours that could combine to form heterostructures with pronounced magnetoelectric effect, thus further advancing and expanding the materials basis for the fast growing field of spintronics research and development.

## Supporting Information

Supplemental Material presents computational details; the structures of Mn@SVG/In<sub>2</sub>Se<sub>3</sub>; additional electronic and magnetic properties of TM decorated graphene and their dependence on the FE polarization of the In<sub>2</sub>Se<sub>3</sub> monolayer; the structures of Mn@SVG/In<sub>2</sub>Se<sub>3</sub> with Mn located between graphene and In<sub>2</sub>Se<sub>3</sub> layers and the corresponding electric structures; the schematic diagram and energy barrier of diffusion for Mn atom crossing the vacancy of graphene from top to interlayer positions in Mn@SVG-P↓-In<sub>2</sub>Se<sub>3</sub> heterostructure; the total magnetic moments and spin moments distributed on Mn and the nearest three carbon atoms; variation of magnetism as a function of artificially increased interlayer distance; dependence of FE controlled magnetic moments on the choice of van der Waals corrections; calculated spin-polarized DOS for 3×3×1 Mn@SVG calculated using the HSE 06 hybrid functional; PDOS shifts in the Cr@SVG/In<sub>2</sub>Se<sub>3</sub> heterostructure; the influence of O<sub>2</sub> and H<sub>2</sub>O molecules on magnetic properties for Mn@SVG/P↓-In<sub>2</sub>Se<sub>3</sub>; and also contains references 1-6.

## Notes

The authors declare no competing financial interest.

## Acknowledgement

We acknowledge the grants of high-performance computer time from computing facility at the Queensland University of Technology, the Pawsey Supercomputing Centre and Australian National Computational Infrastructure (NCI). L.K. gratefully acknowledges financial support by the ARC Discovery Project (DP190101607). Y.G. acknowledges ARC Discovery Project (DP200102546).

## References

1. Feng, Y. P.; Shen, L.; Yang, M.; Wang, A.; Zeng, M.; Wu, Q.; Chintalapati, S.; Chang, C.-R. Prospects of Spintronics Based on 2D Materials. *WIREs Comput. Mol. Sci.* **2017**, 7, (5), e1313..
2. Tang, X.; Kou, L. Two-dimensional Ferroics and Multiferroics: Platforms for New Physics and Applications. *J. Phys. Chem. Lett.* **2019**, 10, (21), 6634-6649.
3. Fert, A. Origin, Development, and Future of Spintronics (Nobel Lecture). *Angew. Chem. Int. Ed.* **2008**, 47, (32), 5956-5967.
4. Hirohata, A.; Takanashi, K. Future Perspectives for Spintronic Devices. *J. Phys. D: Appl. Phys.* **2014**, 47, (19), 193001.
5. Yan, H.; Feng, Z.; Qin, P.; Zhou, X.; Guo, H.; Wang, X.; Chen, H.; Zhang, X.; Wu, H.; Jiang, C.; Liu, Z. Electric-Field-Controlled Antiferromagnetic Spintronic Devices. *Adv. Mater.* **2020**, 32, (12), e1905603.
6. Bader, S. D.; Parkin, S. S. P. Spintronics. *Annu. Rev. Condens. Matter Phys.* **2010**, 1, (1), 71-88.
7. Huang, B.; Clark, G.; Navarro-Moratalla, E.; Klein, D. R.; Cheng, R.; Seyler, K. L.; Zhong, D.; Schmidgall, E.; McGuire, M. A.; Cobden, D. H.; Yao, W.; Xiao, D.; Jarillo-Herrero, P.; Xu, X. Layer-dependent Ferromagnetism in a van der Waals Crystal Down to the Monolayer Limit. *Nature* **2017**, 546, (7657), 270-273.
8. Gong, C.; Li, L.; Li, Z.; Ji, H.; Stern, A.; Xia, Y.; Cao, T.; Bao, W.; Wang, C.; Wang, Y.; Qiu, Z. Q.; Cava, R. J.; Louie, S. G.; Xia, J.; Zhang, X. Discovery of Intrinsic Ferromagnetism in Two-dimensional van der Waals Crystals. *Nature* **2017**, 546, (7657), 265-269.
9. Yi, J.; Zhuang, H.; Zou, Q.; Wu, Z.; Cao, G.; Tang, S.; Calder, S. A.; Kent, P. R. C.; Mandrus, D.; Gai, Z. Competing Antiferromagnetism in a Quasi-2D Itinerant Ferromagnet: Fe<sub>3</sub>GeTe<sub>2</sub>. *2D Mater.* **2017**, 4, (1), 011005.
10. Puthirath Balan, A.; Radhakrishnan, S.; Woellner, C. F.; Sinha, S. K.; Deng, L.; Reyes, C. L.; Rao, B. M.; Paulose, M.; Neupane, R.; Apte, A.; Kochat, V.; Vajtai, R.; Harutyunyan, A. R.; Chu, C. W.; Costin, G.; Galvao, D. S.; Marti, A. A.; van Aken, P. A.; Varghese, O. K.; Tiwary, C. S.; Malie

Madom Ramaswamy Iyer, A.; Ajayan, P. M. Exfoliation of a Non-van der Waals Material from Iron Ore Hematite. *Nat. Nanotechnol.* **2018**, 13, (7), 602-609.

11. K. S. Novoselov, A. K. G., S. V. Morozov, D. Jiang, Y. Zhang, S. V. Dubonos, I. V. Grigorieva, A. A. Firsov. Electric Field Effect in Atomically Thin Carbon Films. *Science* **2004**, 306, 666-669.

12. Candini, A.; Klyatskaya, S.; Ruben, M.; Wernsdorfer, W.; Affronte, M. Graphene Spintronic Devices with Molecular Nanomagnets. *Nano Lett.* **2011**, 11, (7), 2634-2639.

13. Mao, Y.; Yuan, J.; Zhong, J. Density Functional Calculation of Transition Metal Adatom Adsorption on Graphene. *J. Phys. Condens. Matter.* **2008**, 20, (11), 115209.

14. Sielemann, R.; Kobayashi, Y.; Yoshida, Y.; Gunnlaugsson, H. P.; Weyer, G. Magnetism at Single Isolated Iron Atoms Implanted in Graphite. *Phys. Rev. Lett.* **2008**, 101, 137206.

15. Cretu, O.; Krasheninnikov, A. V.; Rodríguez-Manzo, J. A.; Sun, L.; Nieminen, R. M.; Banhart, F. Migration and Localization of Metal Atoms on Strained Graphene. *Phys. Rev. Lett.* **2010**, 105, (19), 196102.

16. Manadé, M.; Viñes, F.; Illas, F. Transition Metal Adatoms on Graphene: A Systematic Density Functional Study. *Carbon* **2015**, 95, 525-534.

17. V. Zólyomi, Á. Ruzsnyák, J. Kürti, and C. J. Lambert. First Principles Study of the Binding of 4d and 5d Transition Metals to Graphene *J. Phys. Chem. C* **2010**, 114, 18548..

18. Bloński, P.; Hafner, J. Geometric and magnetic properties of Pt clusters supported on graphene: Relativistic Density-Functional Calculations. *J. Chem. Phys.* **2011**, 134, (15), 154705.

19. Cao, C.; Wu, M.; Jiang, J.; Cheng, H.-P. Transition Metal Adatom and Dimer Adsorbed on Graphene: Induced Magnetization and Electronic Structures. *Phys. Rev. B* **2010**, 81, (20), 205424.

20. Santos, E. J. G.; Ayuela, A.; Sánchez-Portal, D. First-principles Study of Substitutional Metal Impurities in Graphene: Structural, Electronic and Magnetic Properties. *New J. Phys.* **2010**, 12, (5), 053012.

21. Krasheninnikov, A. V.; Lehtinen, P. O.; Foster, A. S.; Pyykkö, P.; Nieminen, R. M. Embedding Transition-Metal Atoms in Graphene: Structure, Bonding, and Magnetism. *Phys. Rev. Lett.* **2009**, 102, (12), 126807.

22. Quentin M. Ramasse, R. Z., Ursel Bangert, Danil W. Boukhvalov, Young-Woo Son, and Konstantin S. Novoselov. Direct Experimental Evidence of Metal-Mediated Etching of Suspended Graphene. *ACS Nano* **2012**, 6, 4063.

23. Wang, H.; Wang, Q.; Cheng, Y.; Li, K.; Yao, Y.; Zhang, Q.; Dong, C.; Wang, P.; Schwingschlogl, U.; Yang, W.; Zhang, X. X. Doping Monolayer Graphene with Single Atom Substitutions *Nano Lett.* **2012**, 12, (1), 141-144.

24. Lottermoser, T., Lonkai, T. Amann, U., Hohlwein, D., Ihringer, J., Fiebig, M. Magnetic phase control by an electric field. *Nature* **2004**, 430, 541-544.

25. Ederer, C.; Spaldin, N. A. Electric-field-switchable Magnets: The Case of BaNiF<sub>4</sub>. *Phys. Rev. B* **2006**, 74, (2), 020401(R).
26. Chu, Y.-H.; Martin, L. W.; Holcomb, M. B.; Ramesh, R. Controlling Magnetism with Multiferroics. *Mater. Today* **2007**, 10, (10), 16-23.
27. Lee, P. L. a. J. Y. Electrical Control of Magnetization in Narrow Zigzag Silicon Carbon Nanoribbons. *J. Phys. Chem. C* **2009**, 113, 21213.
28. Matsukura, F.; Tokura, Y.; Ohno, H. Control of Magnetism by Electric Fields. *Nat Nanotechnol.* **2015**, 10, (3), 209-220.
29. Ding, W.; Zhu, J.; Wang, Z.; Gao, Y.; Xiao, D.; Gu, Y.; Zhang, Z.; Zhu, W. Prediction of Intrinsic Two-dimensional Ferroelectrics in In<sub>2</sub>Se<sub>3</sub> and Other III<sub>2</sub>-VI<sub>3</sub> van der Waals Materials. *Nat. Commun.* **2017**, 8, 14956.
30. Zhou, Y.; Wu, D.; Zhu, Y.; Cho, Y.; He, Q.; Yang, X.; Herrera, K.; Chu, Z.; Han, Y.; Downer, M. C.; Peng, H.; Lai, K. Out-of-Plane Piezoelectricity and Ferroelectricity in Layered  $\alpha$ -In<sub>2</sub>Se<sub>3</sub> Nanoflakes. *Nano Lett.* **2017**, 17, (9), 5508-5513.
31. Ju, L.; Shang, J.; Tang, X.; Kou, L. Tunable Photocatalytic Water Splitting by the Ferroelectric Switch in a 2D AgBiP<sub>2</sub>Se<sub>6</sub> Monolayer. *J. Am. Chem. Soc.* **2020**, 142, (3), 1492-1500.
32. Gong, C.; Kim, E. M.; Wang, Y.; Lee, G.; Zhang, X. Multiferroicity in Atomic van der Waals Heterostructures. *Nat. Commun.* **2019**, 10, (1), 2657.
33. G. Kresse and Furthmüller J. Efficiency of Ab-initio Total Energy Calculations for Metals and Semiconductors Using a Plane-wave Basis Set. *Comput. Mater. Sci.* **1996**, 6, 15-50.
34. Furthmüller, G. Kresse. Efficient Iterative Schemes for Ab Initio Total-energy Calculations Using a Plane-wave Basis Set. *Phys. Rev. B* **1996**, 54, 11169-11186.
35. Liu, B.; Zhao, X. The synergetic effect of V and Fe-co-doping in TiO<sub>2</sub> studied from the DFT+U first-principle calculation. *Appl. Surf. Sci.* **2017**, 399, 654-662.
36. Piotrowski, M. J.; Ungureanu, C. G.; Tereshchuk, P.; Batista, K. E. A.; Chaves, A. S.; Guedes-Sobrinho, D.; Da Silva, J. L. F. Theoretical Study of the Structural, Energetic, and Electronic Properties of 55-Atom Metal Nanoclusters: A DFT Investigation within van der Waals Corrections, Spin-Orbit Coupling, and PBE+U of 42 Metal Systems. *J. Phys. Chem. C* **2016**, 120, (50), 28844-28856.
37. Han, Z. K.; Gao, Y. Water Adsorption and Dissociation on Ceria-Supported SingleAtom Catalysts: A First-Principles DFT+U Investigation. *Chem. Eur. J.* **2016**, 22, (6), 2092-2099.
38. Robertson, A. W.; Montanari, B.; He, K.; Kim, J.; Allen, C. S.; Wu, Y. A.; Olivier, J.; Neethling, J.; Harrison, N.; Kirkland, A. I.; Warner, J. H. Dynamics of Single Fe Atoms in Graphene Vacancies. *Nano. Lett.* **2013**, 13, (4), 1468-75.
39. Sun, M.; Ren, Q.; Zhao, Y.; Chou, J.-P.; Yu, J.; Tang, W. Electronic and Magnetic Properties of 4d Series Transition Metal Substituted Graphene: A First-principles Study. *Carbon* **2017**, 120, 265-273.

40. Pereira, V. M.; Guinea, F.; Lopes dos Santos, J. M.; Peres, N. M.; Castro Neto, A. H. Disorder Induced Localized States in Graphene. *Phys. Rev. Lett.* **2006**, 96, (3), 036801.
41. Heyd, J.; Scuseria, G. E.; Ernzerhof, M. Hybrid functionals based on a screened Coulomb potential. *J. Chem. Phys.* **2003**, 118, 8207.
42. Yang, K.; Hu, W.; Wu, H.; Whangbo, M.-H.; Radaelli, P. G.; Stroppa, A. Magneto-Optical Kerr Switching Properties of  $(\text{CrI}_3)_2$  and  $(\text{CrBr}_3/\text{CrI}_3)$  Bilayers. *ACS Appl. Electron. Mater.* **2020**, 2, (5), 1373-1380.
43. Thiel, L., Wang Z.; Tschudin, M. A.; Rohner, Gutiérrez-Lezama, D. I.; Ubrig, N.; Gibertini, M.; Giannini, E.; Morpurgo, A. F.; Maletinsky, P. Probing magnetism in 2D materials at the nanoscale with single-spin microscopy. *Science* **2019**, 364, 973-976.